Theory of Atomic-Force Microscopy(STM Theory)

Sci. Rep. RITU A44 (1997) pp. 1-15
No. 1, March 1997

Theory of Atomic-Force Microscopy

Naruo Sasaki and Masaru Tsukada
Department of Physics, Graduate School of Science, University of Tokyo, 7-3-1 Hongo, Bunkyo-ku, Tokyo 113, Japan

(Received January 21, 1997)

The mechanism of force detection of Atomic-Force Microscopy (AFM) is theoretically investigated. First, a theoretical simulation of contact AFM images is performed, and a tip apex structure is studied. It is clarified how the AFM images and the force distributions change as the load varies. It is also revealed that the characteristics of the AFM images such as their detailed microscopic pattern, the symmetry, and the corrugation amplitude, depend strongly on the tip apex structure. Secondly, fundamental features of the atomic-scale friction in Frictional-Force Microscopy (FFM) are studied. Simulated FFM images are in good agreement with observed ones. Then we discuss the mechanism of the image pattern of FFM by an analytical method. It is revealed that the part of the boundary of the stable region of the cantilever basal position, appears as the boundary between the bright and the dark area of FFM images. Thus we clarify the physical meaning of the FFM image patterns. Lastly, we studied dynamics of the large amplitude cantilever oscillations in the noncontact AFM (nc-AFM). The oscillation of the cantilever is treated as a forced oscillation periodically interrupted by collisions with the surface. By solving this extremely nonlinear problem numerically, some remarkable features of the cantilever oscillation are revealed. We observed strange behaviors of the cantilever such as a bimodal state of dynamical touching and non-touching motion, as well as a fractional resonance features.

KEYWORDS: AFM, FFM, contact, friction, noncontact, forced vibration, tip, cantilever, graphite, Lennard-Jones potential

1. Introduction

Among various sorts of scanning probe microscopies (SPM), Atomic-Force Microscopy (AFM) [1] is a powerful method for the determination of surface structures, because it can resolve both conducting and insulating surfaces in an atomic-scale. Therefore AFM has become a basic experimental device not only in the field of surface science but also in many other basic and applied fields such as semiconductor devices, catalyses, electrochemistry and biological science. However the microscopic mechanism of AFM has not been clarified yet. Therefore, in this article, we investigate systematically the mechanism of force detection of AFM and give a physical interpretations of AFM images.

First, in Section 2, we focus on "contact AFM". The principle of contact AFM is detecting a force exerted between a tip apex mounted on a cantilever and a sample surface. The force is directly detected by measuring the static cantilever deflection. Here we perform overall studies on the effect of the tip apex structure on contact AFM. The detailed feature of the force distributions between the tip and surface, effect of the tip apex tilting, and influence of the orientation, are clarified. [2, 3]

When contact AFM is used in the measurament of friction, it is called "Frictional-Force Microscopy (FFM)", which has enabled us to observe the atomic-scale friction, [4] and has opened a new research area of friction — nanotribology. Therefore FFM is a powerful tool for understanding the basic friction mechanism between a single asperity and an atomically flat surface. However, from a theoretical view point, the basic issue, *i.e.*, 'what kind of physical information is included in FFM images ?', has not been fully discussed yet. Therefore, in Section 3, we simulate FFM images numerically based on a static model, and compare them with experimental results. [5–8] Then we will provide a comprehensive physical interpretation of FFM image patterns, by using an analytical method. [9] Based on the analysis of the sticking region of the tip atom position, the 'sticking domain' of the tip atom is clearly defined. The quasi stable equilibrium condition can be rewritten as a mapping relation between the tip atom position (x, y) and the cantilever basal position (x_s, y_s), which provides an important clue for an understanding of the FFM image.

Recently "noncontact AFM (nc-AFM)" [10] has been developed, the operating condition of which is quite different from those in contact AFM and FFM. In this mode, the cantilever is forced to oscillate near its resonant frequency. At the stable oscillation state, the tip height which keeps the resonance frequency or oscillation amplitude constant, is monitored during the scan. From this information one obtains the nc-AFM image which, in a certain condition, achieves an atomic-scale resolution. Noncontact AFM is expected as a non-destructive method of measurement of the sample surface, and has succeeded to observe atomic-scale images of them. However the mechanism of this nc-AFM has not been clarified at all. For example, so far, it has not been studied what physical quantities are actually obtained by the tip to form the image. Therefore, as the first step toward an understanding of the force-detecting mechanism of the nc-AFM, we performed a preliminary study of a large

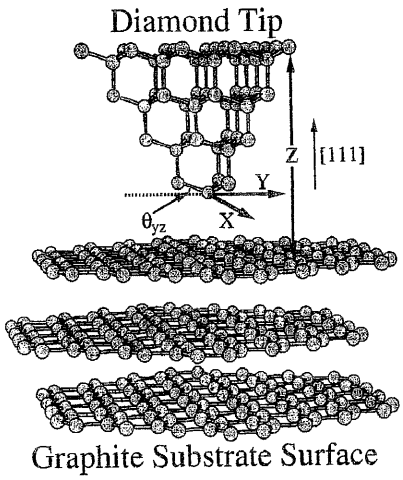

Figure 1. Contact AFM system of the diamond [111] tip made up of 54 atoms and the graphite surface. Z denotes the vertical distance between the fixed basal plane of the tip and the first layer of the surface before relaxation. θ_{xy} is a tilt angle of the tip.

amplitude movement of the cantilever. Dynamics of the cantilever in nc-AFM is discussed in Section 4.

2. Effect of the tip structure on contact AFM

2.1. Cluster model of the contact AFM system

The tip-surface system of contact AFM is represented by the cluster model composed of the multiple-atom diamond [111] tip comprised of 54 atoms and the graphite sample surface, as shown in Figure 1. In the simulation, another multiple-atom diamond [111] tip made up of 50 atoms as shown in Figure 2 is also used. Any possible effects of the reconstruction of the tip surface are neglected. Considering the symmetry, the cluster model of the graphite surface is formed by adding hexagons around the center hexagon. If the surface deformation near the tip-surface contact region is noticed, the small surface cluster with 96 cluster atoms per layer is enough for the AFM simulations. Therefore, as a cluster of the sample surface, the graphite made up of 288 atoms with three layers, each of which consists of 96 atoms, is used. As a boundary condition, all of the 96 atoms of the third layer, and 42 atoms on the edges of the first and the second layers are fixed. Following the standard nomenclature of bulk graphite, the atomic site of the first layer just under which there exists an atom or not is designated as the A or the B site, respectively. And the center of the hexagon is called the H site.

Then, model potential energy we use in the simulation is explained. The total energy V of the system consists of the potential energy of the tip V_T, that of the sample surface V_S and the tip-surface interaction V_{TS} as follows:

$$\begin{aligned} V(\{\mathbf{r}_{\rm tip}\},\{\mathbf{r}_{\rm surf}\}) &= V_T(\{\mathbf{r}_{\rm tip}\}) + V_S(\{\mathbf{r}_{\rm surf}\}) \\ &+ V_{TS}(\{\mathbf{r}_{\rm tip}\},\{\mathbf{r}_{\rm surf}\}), \end{aligned} \quad (1)$$

where $\{\mathbf{r}_{\rm tip}\}$ and $\{\mathbf{r}_{\rm surf}\}$ are the positions of the tip atoms and the sample surface atoms, respectively.

First, V_T is assumed to be a simple harmonic potential for the diamond [11]. It is expressed as the sum of two

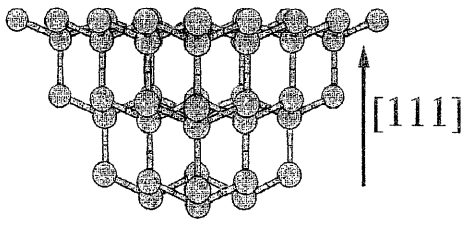

Figure 2. Multiple-atom tip made up of 50 atoms.

different types of harmonic terms as follows:

$$V_T(\{\mathbf{r}_{\rm tip}\}) = \frac{1}{2}\sum_{i-j}\lambda_r(r_{ij}-r_0)^2 + \frac{1}{2}\sum_{i-j-k}\lambda_\theta r_0^2(\theta_{ijk}-\theta_0)^2. \quad (2)$$

Here the indices of the summation i-j and i-j-k represent the nearest-neighbor bonds and bond pairs, respectively. Therefore the first term means the bond-stretching energy due to the change of each nearest neighbor bond length, r_{ij} from the equilibrium one, r_0. Furthermore the second term represents the bond-bending energy corresponding to the change of each bond angle, θ_{ijk} from the equilibrium one, θ_0. The parameters of V_T are $r_0 = 1.5445$Å, $\lambda_r = 29.512\,\mathrm{eV/Å^2}$, $\theta_0 = \cos^{-1}(-1/3)\,\mathrm{rad}$ and $\lambda_\theta = 3.5213\,\mathrm{eV/Å^2}$.

Similarly, V_S is also assumed to be a harmonic potential for the graphite [12], which consists of four different types of harmonic terms as follows:

$$\begin{aligned} V_S(\{\mathbf{r}_{\rm surf}\}) &= \frac{1}{2}\sum_{i-j}\mu_r(r_{ij}-r_0)^2 \\ &+ \frac{1}{2}\sum_{i-j-k}\mu_\theta r_0^2(\theta_{ijk}-\theta_0)^2 \\ &+ \frac{1}{2}\sum_{i-j:\mathrm{interlayer}}\mu_d(d_{ij}-d_0)^2 \\ &+ \frac{1}{2}\sum_{i-(j,k,l)}\mu_p\left(\delta z_i - \frac{\delta z_j+\delta z_k+\delta z_l}{3}\right)^2 \end{aligned} \quad (3)$$

Similar to V_T, the first and the second terms correspond to the bond-stretching, and the bond-bending energy, respectively. In this case, θ_{ijk} denotes the angle between the bond i-j and the bond j-k within the same honeycomb net plane. Unlike V_T, V_S has the third and the forth terms. The indices of the summation 'i-j: interlayer' and i-(j,k,l) represent the interlayer bond, and bond triplets, respectively. The third term is the interlayer bond-stretching energy for the change of the interlayer distance, d_{ij} from the equilibrium distance, d_0. The fourth term is the bending energy of the local planar structure due to the normal displacement of the ith atom from the coplanar position with respect to the three neighboring atoms j,k and l; δz_i denotes the normal displacement of the ith atom from the initial position. The parameters of V_S are assumed as $r_0 = 1.4210$ Å, $\mu_r = 41.881\,\mathrm{eV/Å^2}$, $\theta_0 = 2\pi/3$ rad, $\mu_\theta = 2.9959\,\mathrm{eV/Å^2}$, $\mu_d = 0.34765\,\mathrm{eV/Å^2}$, $d_0 = 3.3539$ Å and $\mu_p = 18.225\,\mathrm{eV/Å^2}$, respectively.

The sum of the 6-12 Lennard-Jones potential is chosen for V_{TS}, *i.e.*,

$$V_{TS}(\{\mathbf{r}_{\rm tip}\},\{\mathbf{r}_{\rm surf}\}) = \sum_{i,j} v_{TS}\left(|\mathbf{r}_{{\rm tip},i} - \mathbf{r}_{{\rm surf},j}|\right)$$

$$= \sum_{i,j} 4\epsilon\left[\left(\frac{\sigma}{r_{ij}}\right)^{12} - \left(\frac{\sigma}{r_{ij}}\right)^{6}\right]. \quad (4)$$

Here, we assume that every tip atom interacts with all the surface atoms only through a pair potential and that this potential is the same for all the pairs of the tip and the sample surface atoms. Although the parameters ϵ and σ are not necessarily unique, those used by Gould *et al.*, [13]—$\epsilon = 0.87381 \times 10^{-2}$ eV and $\sigma = 2.4945$ Å are employed. The merit of this potential is that the corrugation amplitude is well reproduced [2, 3, 13]. This potential is used with a cutoff at $r_c = 2.3\sigma$.

2.2. Method of simulation

In this section, the method of simulation is explained. Atoms in the AFM system are assumed to be always located at a stable equilibrium state, and the adiabatic theorem holds good. This assumption is valid because the cantilever scanning speed in experiment, v_{AFM}, is almost in the limit of zero, compared to the velocity of lattice vibration v_{L}. In most of AFM experiments, $v_{\mathrm{AFM}} \sim 10^{-11}$-$10^{-8}$ m/s, while $v_{\mathrm{L}} \sim 10^{3}$-$10^{4}$ m/s.

After the tip basal plane is fixed at a certain position above the sample surface, the total energy $V(\{\mathbf{r}_{\mathrm{tip}}\}, \{\mathbf{r}_{\mathrm{surf}}\})$ is minimized to relax the sample surface by using the Polak-Ribiere–type conjugate gradient (CG) method [14]. Then, total force $\boldsymbol{F}(z)$ acting on the tip is obtained for the respective values of z. Here z is the coordinate parallel to [111] axis of the diamond, that is to say, perpendicular to the graphite [0001] plane, as shown in Fig. 1. In the calculation of AFM, only the perpendicular deflection of the cantilever is allowed, and we focus on the z component of $\boldsymbol{F}(z)$, $F_z(z)$.

Here we set the convergence criterion as follows: the maximum of absolute values of all the forces acting on the movable atoms is lower than 10^{-5} nN, *i.e.*

$$\max_{1\le i\le N}(|\boldsymbol{F}_i|) < 10^{-5}\mathrm{nN}, \quad (5)$$

where N is the total number of movable atoms both of the tip and the sample surface, and $\boldsymbol{F}_i$ is a force acting on the ith atom.

We performed calculations as mentioned above for several values of z for a fixed lateral (x, y). Further, according to the method adopted by Tang *et al.* [15], z-F_z relation (force curve) is obtained by a polynomial fit from the calculated values of F_z corresponding to these z values. The six order polynomial is used and the residue of this fitting is less than the order of 10^{-5} nN. Then the equation

$$F_z(z) = F_{\mathrm{sc}}, \quad (6)$$

is solved and the tip height z for the scanning force F_{sc} is calculated. If this procedure is repeated for each (x, y) value in the region of the tip scanning, the AFM image

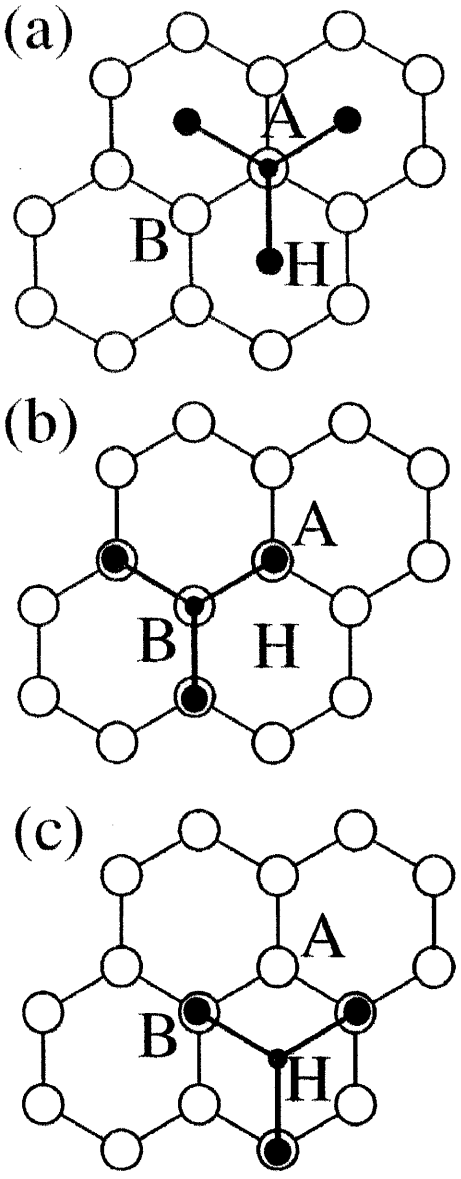

Figure 3. Multiple-atom tip made up of 54 atoms positioned on the (a) A, (b) B, and (c) H sites. The small and the large black circles correspond to the first- and the second-layer tip atoms, respectively. The white circles correspond to the graphite atoms.

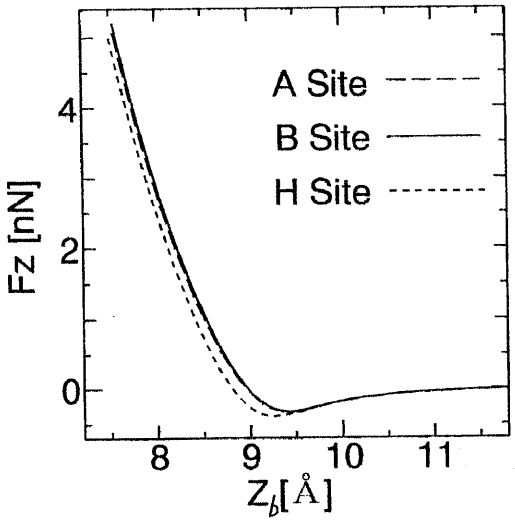

Figure 4. Force-distance curves on the A, B and H sites for a multiple-atom tip made up of 54 atoms.

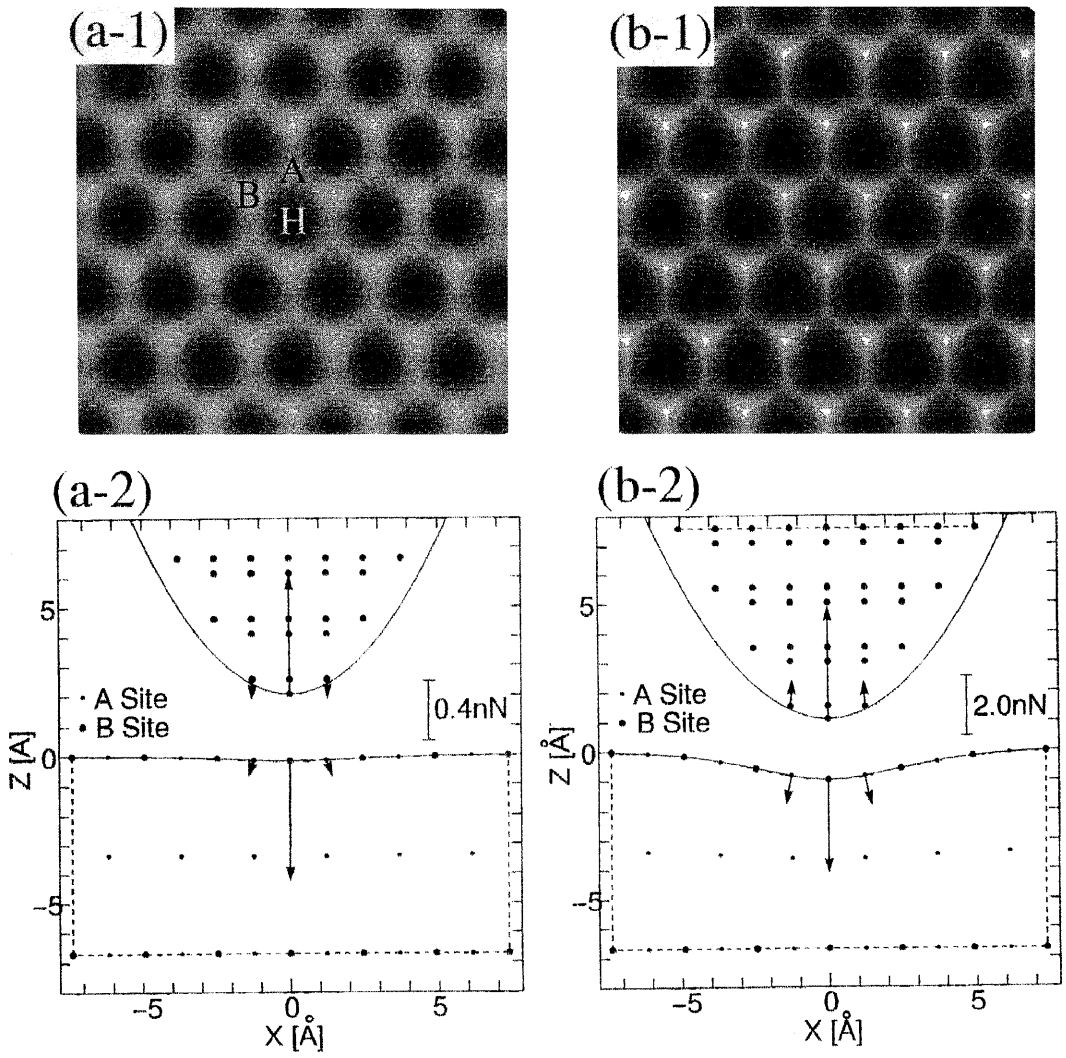

Figure 5. (a) Constant-force images and (b) force distributions for a multiple-atom tip made up of 54 atoms. In (a-1) and (b-1), the lateral dimensions are 13 Å × 13 Å. In (a-2) and (b-2), the tip is placed right above the B site. The larger black circles represent surface B sites or tip atoms, and the smaller black circles represent surface A sites. The solid curve denotes the section of the paraboloid that includes four tip apex atoms. The broken lines denote the boundary of the cluster models.

with a constant scanning force F_{sc} can be calculated. On the other hand, when z is fixed, the constant-height image is obtained by the values of $F_z(z)$ over the (x, y) domain.

2.3. Multiple-atom tip made up of 54 atoms

One of two multiple-atom tips is made up of 54 atoms with the axis parallel to the diamond [111] direction. This tip consists of eight layers, and has one apex atom and three atoms in the second layer as shown in Fig. 1. The tip orientation is fixed as shown in Figures 3(a)-3(c). In this orientation, the calculated force - distance curves are presented in Figure 4. We note that z_b is defined as a position of the fixed basal plane of the diamond tip. It is shown that the H site is lower than the A and the B sites, and that the B site is a little higher than the A site. The reason for the difference of the height between the three sites is explained below, with the interpretations of AFM images.

The tip detects forces mainly by one apex atom and by three atoms of the second layer as seen in Figures. 5(a-2) and 5(b-2). In a weak repulsive force of $F_z = 0.5$ nN, one apex atom detects the dominant repulsive forces, and three atoms of the second layer feel rather small attractive forces as shown in Fig. 5(a-2). Therefore, the forces between the tip and the surface approximately concentrate only on one atom of the tip and the surface, and the single-atom contact occurs. However, as F_z increases, repulsive forces distribute over many atoms. In a strong repulsive force of $F_z = 5.0$ nN, the forces felt by three atoms of the second layer also become repulsive and larger, and multiple-atom contact occurs as seen in Fig. 5(b-2). However, the image reflects the periodicity of the graphite lattice and has an apparent atomic resolution [Fig. 5(b-1)]. Both AFM images of Fig. 5(a-1) and Fig. 5(b-1) correspond well to the experimental ones [16, 17].

Although the interpretation of the calculated images

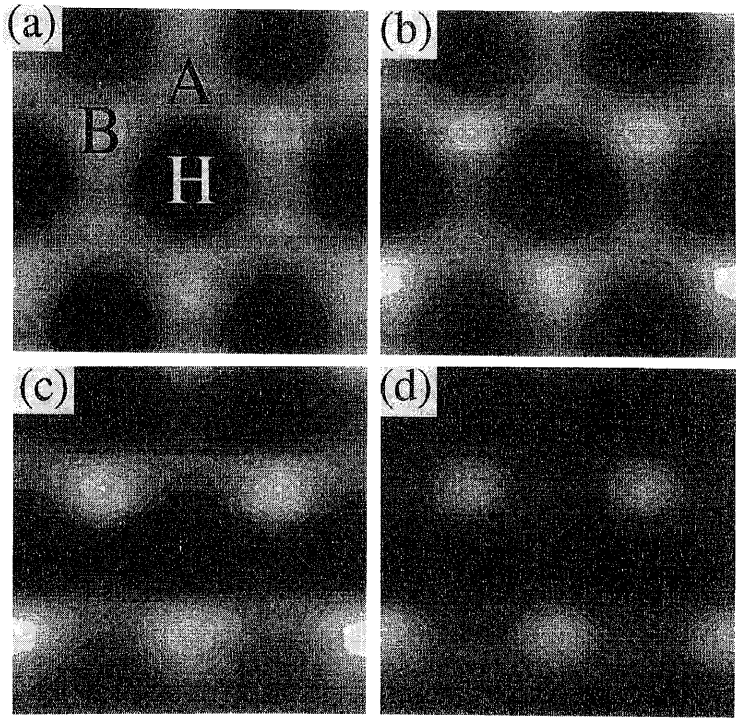

Figure 6. Constant-force images for a multiple-atom tip made up of 54 atoms with the scanning force of 0.1 nN. The tilt angle θ_{yz} is (a) 19.5°, (b) 10°, (c) 5°, and (d) 0°. The lateral dimensions are 5 Å × 5 Å.

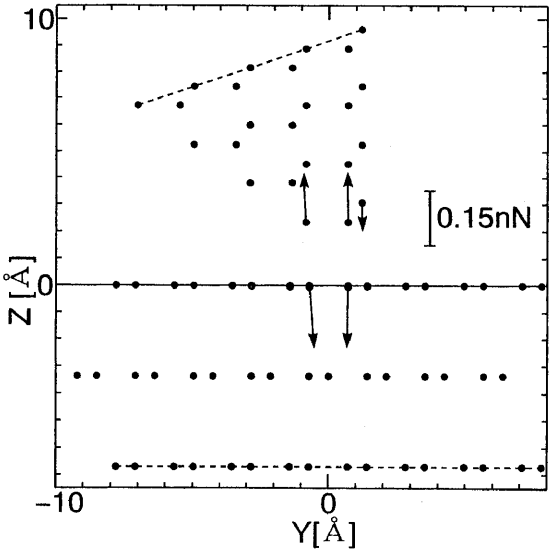

Figure 7. Force distributions for a weak repulsive force of $F_z = 0.1$ nN when the tilt angle θ_{yz} is 0°. The y and z coordinates of the atomic sites and of the forces are presented.

is generally difficult, the brightness of the site in the particular example mentioned above can be qualitatively explained by the location of the tip atoms. For the case of $F_z = 0.5$ nN, the simulated image shows basically a honeycomb lattice pattern, in which the B site is a little brighter than the A site if we look at the image of Fig. 5(a-1) closely. When the tip is placed above the A site, three atoms of the second layer of the tip are located above neither the A site nor the B site as shown in Fig. 3(a).

Therefore, the attractive forces between the surface and the second layer of the tip, obtained when the tip is placed above the A site, becomes larger than those obtained when the tip is situated above the B site [Fig. 3(b)]. However, the repulsive force between the surface and the tip apex atom above the A site is almost equivalent to that above the B site. Therefore, the net repulsive force above the B site is larger than that above the A site. With the increase of F_z, the bright spots tend to form a triangular shape, as seen in the case of $F_z = 5.0$ nN. At the same time, a wire net pattern combining the A and the B sites is also emerged as seen in Fig. 5(b-1). When the tip is placed above the B site, each of the three tip atoms of the second layer can easily interact with the A site as shown in Fig. 3(b). In this location, the repulsive forces between the surface and the second layer of the tip become the largest. Furthermore, the effect of the interlayer interaction becomes more enhanced in the case of Fig. 5(b-1) than the case in Fig. 5(a-1). Thus, the net repulsive forces above the B site are larger than those above the A site. In this strong repulsive force mode, the physical quantity represented by the AFM image is the sum of the forces distributed over many atoms that are self-consistently determined, together with the microscopic atomic deformations of both the tip and the surface. Therefore its correspondence with the surface corrugation is rather complicated and a simple explanation is rather difficult.

The corrugation amplitude $\triangle z_{\mathrm{BH}}$ (the difference in the tip height between the B and the H sites) is about 0.14 Å for Fig. 5(a-1), and 0.08 Å for Fig. 5(b-1). One of the reason why the corrugation for the stronger repulsive force is smaller than that for the weaker repulsive force is probably that the edge effect is not negligible for the multiple-atom tip even at $F_z = 5.0$ nN. Another reason is due to the structure of the tip apex.

The effects of the tip apex structure on the image are also investigated by the tilt of the tip. The tilt of the tip causes a change of the effective tip apex geometry which influences the net forces between the tip and the surface. The tip is tilted around the axis parallel to the x axis passing the tip apex atom. The tilt angle is denoted as θ_{yz} presented in Fig. 1, and it is varied from 19.5° to 0°. At the respective θ_{yz}, the tip is scanned with a constant force of 0.1 nN. At $\theta_{yz} = 19.5°$, an effective tip is composed of one apex atom and three atoms in the second layer, and it has threefold symmetry. On the other hand, when $\theta_{yz} = 0°$, the tip consists of two apex atoms and two second layer atoms, and it has approximately the twofold symmetry. Corresponding to this change of the tip apex symmetry, the threefold symmetry of AFM images also turns into the twofold symmetry as shown in Figures 6(a)-6(d) in the order of θ_{yz} = (a)19.5°, (b)10°, (c)5° and (d)0°. With the decrease of θ_{yz}, the A sites

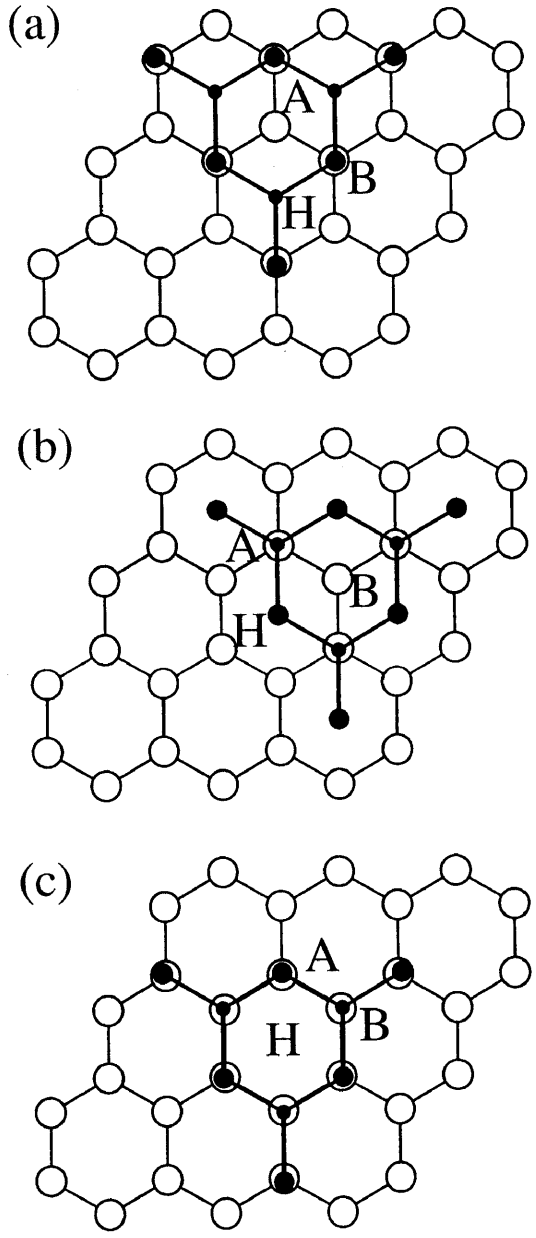

Figure 8. Multiple-atom tip made up of 50 atoms positioned on the (a) A, (b) B, and (c) H sites.

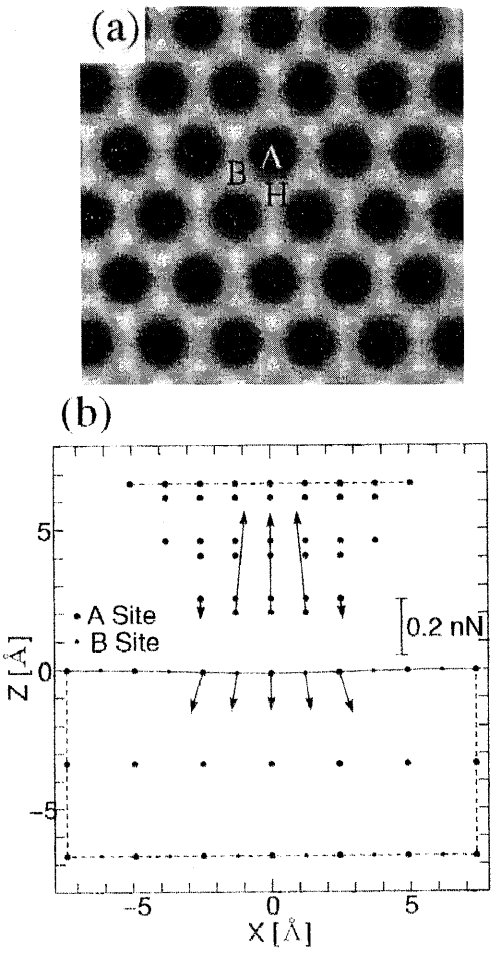

Figure 9. (a) Constant-force image and (b) force distributions for a multiple-atom tip made up of 50 atoms. F_z is a weak repulsive force of 0.5 nN. In (a), the lateral dimensions are 13 Å × 13 Å. In (b), the multiple-atom tip is placed right above the A site. Only the x and z components of the atomic sites and the forces are shown. The larger black circles represent surface A sites or tip atoms, and the smaller black circles represent surface B sites. The broken lines denote the boundary of the cluster models.

become darker and the stripes along the x-direction become brighter. Fig. 6(d) is obtained because the forces are distributed dominantly on two apex atoms of the tip as shown in Figure 7. This image corresponds well to the experimental images [17, 18].

2.4. Multiple-atom tip made up of 50 atoms

The other model of a multiple-atom tip is made up of 50 atoms with the axis parallel to the [111] axis. This tip consists of six layers, and has three apex atoms on the top layer and six atoms in the second layer as presented in Fig. 2. Therefore it is a rather dull tip. The tip orientation is fixed as shown in Figures 8(a)-8(c).

This tip detects forces mainly by three apex atoms and by six atoms of the second layer [Figure 9(b)]. The image of the graphite surface with a scanning force of 0.5 nN shows a honeycomb lattice [Fig. 9(a)]. In this image, both the B and the H sites are brighter than the A sites. Similar to the case of the tip made up of 54 atoms, the brightness of the site is explained as follows: When the tip is placed above the H site, the three first-layer atoms and the six second-layer atoms easily interact with the B and the A sites respectively [Fig. 8(c)]. Above the B site, only three apex atoms significantly interact with the A sites [Fig. 8(b)]. However, when the tip is placed above the A site, only six atoms of the second layer are located above the B sites [Fig. 8(a)]. Therefore, the repulsive tip-surface interaction above the B and the H sites becomes larger than that for the case with the tip placed above the A site. The corrugation amplitude Δz_{HA} is 0.14 Å, and the H site is as bright as the B site. Thus, although the multiple-atom contact occurs, even the rather dull tip can observe a honey-

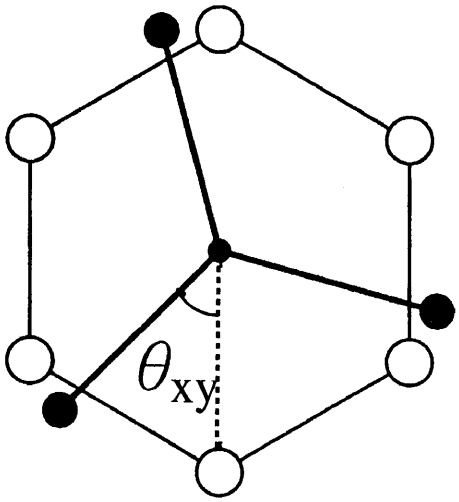

Figure 10. The rotational angle θ_{xy} of the tip. The smaller black circles denote the tip apex atoms and the larger black circles denote the atoms of the second layer of the tip. The white circles denote surface atoms.

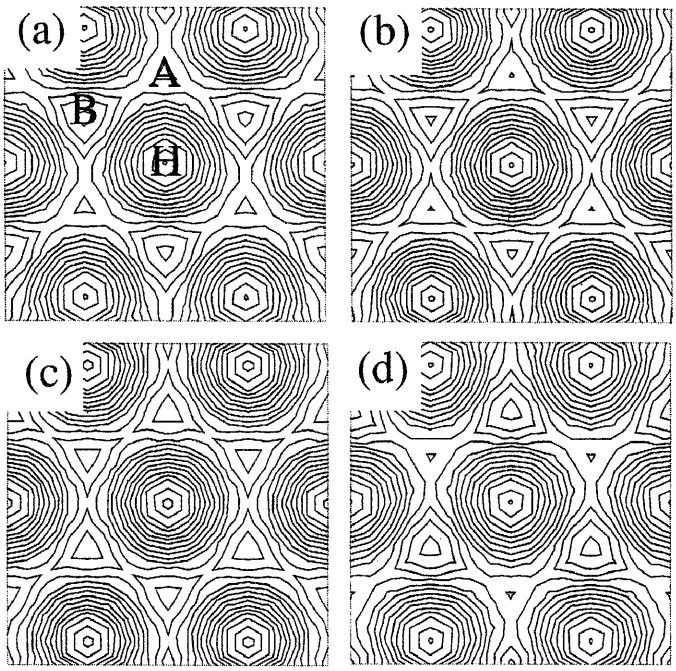

Figure 11. Constant-force[F_z = 0.5 nN] images for contour-plot expressions obtained by the multiple-atom tip made up of 54 atoms. Thick curves denote the boundaries of the bright spots of the A or the B site. The rotational angle θ_{xy} is (a) 0°, (b) 20°, (c) 30°, and (d) 60°. The lateral dimensions are 5 Å × 5 Å.

comb lattice. Unlike the image of the single-atom tip, the bright spots do not match the real atomic sites any longer. Although the A sites are atomic sites, the image of the A sites is dark. This dull tip observes the forces distributing over a wider region than the multiple-atom tip made up of 54 atoms as shown in Fig. 9(b). However, in the orientation mentioned above, the projection of the tip apex to the surface is nearly commensurate with the graphite lattice, and eventually the honeycomb image is obtained. Therefore, this image of Fig. 9(b) reflects the periodicity of the graphite lattice. We should be careful that the periodic AFM images can be always obtained with an unusual tip as used here, if the surface has an ideal two-dimensional translational symmetry. Thus the tip apex structure is an important factor in determining the contact condition and the region of force distributions.

2.5. Tip orientation

In this section, the effects on the AFM image of the tip rotation around its axis are investigated for two kinds of multiple-atom tips; 1) 54-atom tip which has one apex atom and three atoms in the second layer, and 2) 50-atom tip which has three apex atoms and six atoms in the second layer. First, we will discuss the results for the multiple-atom tip made up 54 atoms. When the tip is rotated clockwise around the [111] axis parallel to the z axis with a scanning force of 0.5 nN [Figure 10], the image varies as shown in Figures 11(a)-11(d). The definition of θ_{xy} is illustrated in Fig. 10. At $\theta_{xy} = 0°$, the B site is brighter than the A site [Fig. 11(a)], and the corrugation amplitude is about 0.13 Å. As θ_{xy} increases, the difference of the brightness between the A and the B sites decreases [Fig. 11(b)]. At $\theta_{xy} \simeq 30°$, the A site is approximately as bright as the B site and the image becomes a nearly perfect honeycomb lattice pattern [Fig. 11(c)]. In our calculation, the precise angle where the A site is exactly as bright as the B site is about 27°. When θ_{xy} increases still more, the A site becomes brighter than the B site and the corrugation amplitude becomes larger and takes the maximum value, 0.15 Å at $\theta_{xy} \simeq 35°$. These results show the mechanical inequality between the A and the B sites based on the interlayer interaction. At $\theta_{xy} = 60°$, the brightness of the A and the B sites is perfectly reversed compared to the case of $\theta_{xy} = 0°$ [Fig. 11(d)], and the corrugation is about 0.14 Å. Thus AFM images reflect the rotation of the tip for 60°, and the rotation causes the reverse of the site brightness between the A and the B sites. This reverse is caused mainly by the interaction between three second layer atoms of the tip and the surface sites.

Next, the rotation of the multiple-atom tip made up of 50 atoms is discussed. This tip has three atoms on the truncated plane of its apex. The influence of the tip orientation is rather different from that for the tip made up of 54 atoms. The tip is also rotated clockwise around [111] axis with a scanning force of 0.1 nN. The image varies as shown in Figures 12(a)-12(c). For this tip, the brightness between the A and the B sites for $\theta_{xy} = 60°$ is also perfectly reversed compared to that for $\theta_{xy} = 0°$, similar to the case of the tip made up of 54 atoms. However, variation of the corrugation amplitude for a 50-atom tip is much larger than that for a 54-atom tip. At $\theta_{xy} = 0°$, the tip is nearly commensurate

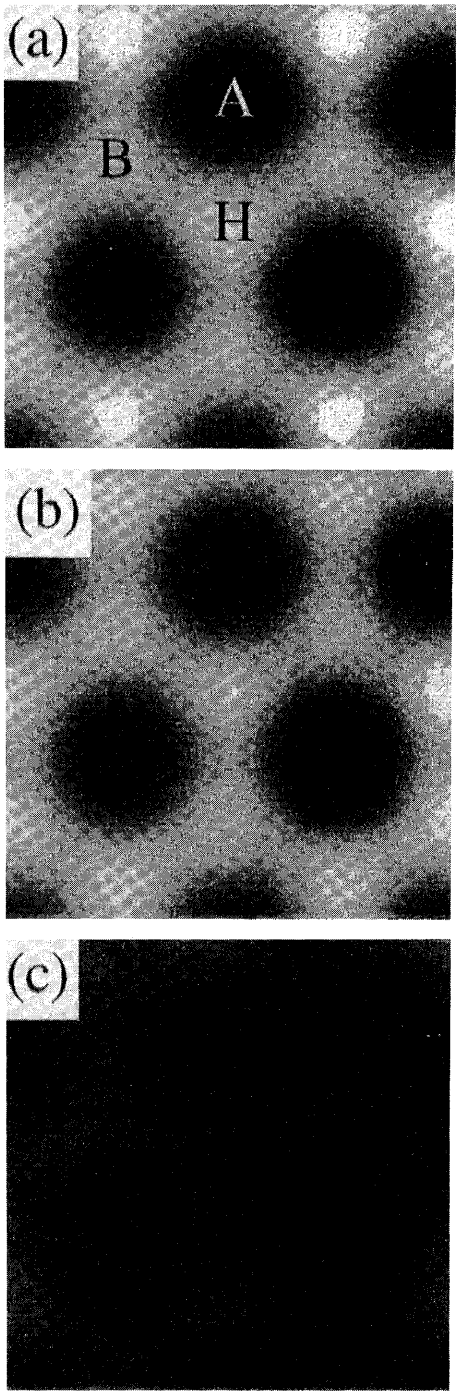

Figure 12. Constant-force[F_z = 0.1 nN] images for gray-scale expressions obtained by the multiple-atom tip made up of 50 atoms. The rotational angle θ_{xy} is (a) 0°, (b) 10°, and (c) 20°. The lateral dimensions are 5 Å × 5 Å.

with the surface and the honeycomb image is obtained as shown in Fig. 12(a). In this case, the corrugation amplitude is about 0.17 Å. However, when θ_{xy} increases, the tip apex structure becomes incommensurate with the surface, and the corrugation amplitude becomes smaller. At $\theta_{xy} = 10°$, the corrugation of the image changes a little [Fig 12(b)]. However, at $\theta_{xy} = 20°$, the corrugation

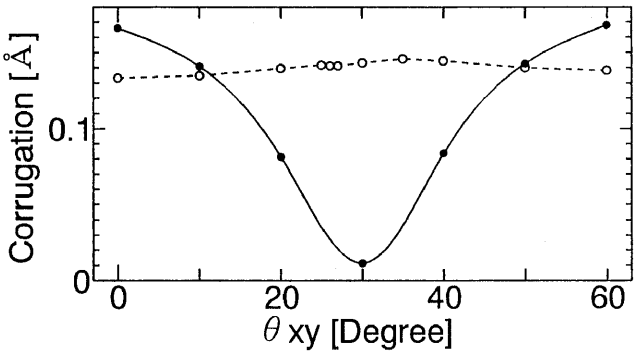

Figure 13. Corrugation amplitude as a function of the rotational angle θ_{xy} for (a) 54-atom tip under the constant scanning force of F_z = 0.5 nN (white circles and dotted curves), and (b) 50-atom tip under F_z = 0.1 nN (black circles and solid curves).

rapidly decreases and the image becomes rather dark [Fig 12(c)]. At $\theta_{xy} \simeq 30°$, the tip apex structure becomes the most incommensurate with the surface and the corrugation takes the minimum–0.01 Å. Therefore, although the image still has a threefold symmetry, it can be thought that the image obtained around this orientation cannot be observed in the experiment [Fig. 12(c)]. This restricts the region of rotation angle for observing the AFM images, and the region in which AFM images are impossible to obtain appears at every 60°.

The corrugation amplitude as a function of the tip orientation (θ_{xy}) is presented in Figure 13. The difference between the maximum and the minimum corrugation for the tip made up of 54 atoms–0.01 Å–is much smaller than that for the tip made up of 50 atoms. Thus, the AFM image is sensitive to the tip rotation. Moreover, the sensitivity of the image to the tip orientation depends strongly on the tip apex structure.

3. Atomic-scale friction in FFM

3.1. Cluster model of FFM system

In the numerical simulation of FFM, a single-atom tip connected with a cantilever is scanned on a rigid monolayer graphite surface. Figure 14(a) schematically represents the cluster model of the FFM system. In the simulation, only the small loading condition is treated. Therefore, under this low loading condition, the surface deformation is very small, and the effect of the second layer of graphite can be neglected. This is why a second layer of graphite is not necessary. The model of the graphite monolayer surface consists of 600 carbon atoms and 271 hexagons, and the lattice constant of the graphite is assumed to be 1.421 Å. In this case, the range of the tip scan must be limited near the center of the surface model, in order to avoid any of the artificial boundary effects. The total potential energy V is assumed to consist of the elastic energy of the cantilever V_T, and the microscopic tip-surface interaction V_{TS}. This relation can be written as follows:

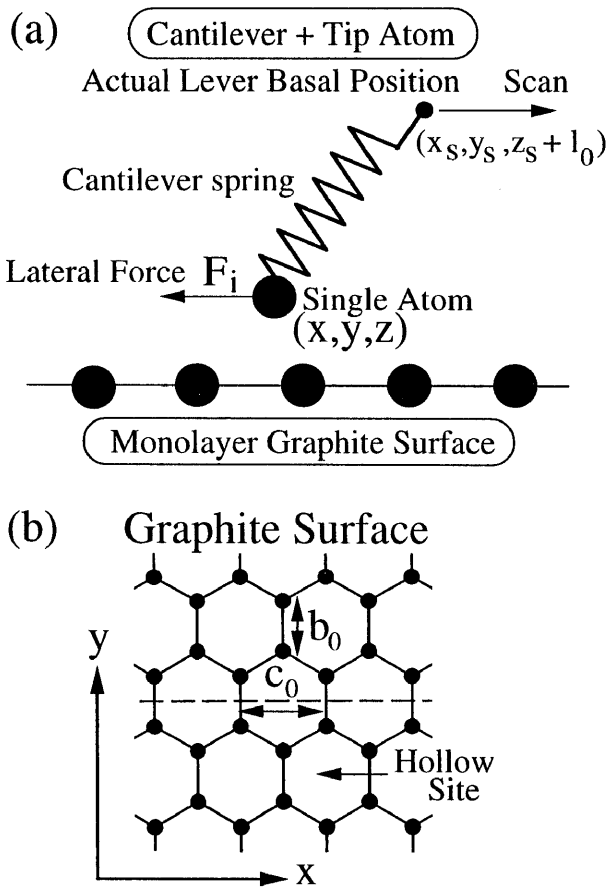

Figure 14. (a) Schematic illustration of the FFM system used in our calculation. The single-atom tip connected with the cantilever spring is scanned on a rigid monolayer graphite surface. (b) Lattice structure of the graphite. c_0 is the length of a unit translational vector of graphite. b_0 is the C-C bond length of graphite. $c_0 = 2.46$ Å, and $b_0 = 1.42$ Å.

$$V(\{\mathbf{r}_{\rm tip}\}) = V_T(\{\mathbf{r}_{\rm tip}\}) + V_{TS}(\{\mathbf{r}_{\rm tip}\}) , \tag{7}$$

where $\{\mathbf{r}_{\rm tip}\} = (x, y, z)$ denotes the actual tip atom position. Here, the x and the y directions parallel to the surface are defined as shown in Fig. 14(b), and the z axis is perpendicular to the surface, $x - y$ plane. The origin of the z axis is defined as the position of the graphite surface.

The cantilever is mimicked by an equivalent three-dimensional spring, and V_T is assumed to be harmonic as follows:

$$V_T(\{\mathbf{r}_{\rm tip}\}) = \frac{1}{2} \sum_{i=x,y,z} k_i (x_i - x_{si})^2, \tag{8}$$

where $k_i (i = x, y, z)$ is an elastic constant of the cantilever spring parallel to the $i (i = x, y, z)$ direction. This spring is also assumed to include the effect of the microscopic interatomic bonds of the tip. And (x_s, y_s, z_s) denotes the equilibrium position of the tip atom for the system without the interaction with the surface. The vertical component k_z is assumed to be 0.25 N/m, which is of the same order as realized in most of the experiments. k_x and k_y are treated as parameters.

Tip-surface interaction V_{TS} can be obtained as the sum of all the pair interactions between the single-atom tip and the sample surface atoms. The Lennard-Jones potential mentioned in Section 2.1, is employed here as follows:

$$V_{TS}(\{\mathbf{r}_{tip}\}) = \sum_i 4\epsilon \left[\left(\frac{\sigma}{r_{0i}} \right)^{12} - \left(\frac{\sigma}{r_{0i}} \right)^{6} \right]. \tag{9}$$

Here, r_{0i} is the distance between the tip atom and the ith atom in the graphite surface, and the parameters are just the same as those mentioned in Section 2.1: $\epsilon = 0.87381 \times 10^{-2}$ eV, and $\sigma = 2.4945$ Å.

The simulation has been performed under the constant-height mode. Therefore, (x_s, y_s) is varied with the lever basal position along the z direction fixed under the repulsive-force condition, and the FFM system comprised of the tip and the surface, is totally relaxed for each (x_s, y_s), based on the CG method mentioned in Section 2.2. Then the optimized position of the tip atom (x, y, z), and the lateral force $F_i (i = x, y)$ acting on the lever basal position are obtained. The lateral force F_i acting in the $-i$ direction, as defined in Fig. 14(a), is given by

$$F_i = \left. \frac{\partial V_{tot}}{\partial x_i} \right|_{(x,y,z)=(x_s,y_s,z_s)} \quad (i = x, y). \tag{10}$$

3.2. Tomlinson's mechanism

In the simulation, we assume that the friction on an atomic-level is originated based on Tomlinson's mechanism [19]. Therefore in this section, Tomlinson's mechanism is described in detail. First, the following two conditions are assumed: (1) The tip-surface system is considered under the condition of the absolute zero temperature $T = 0$ K. In this case, thermal activated processes can be perfectly neglected. (2) FFM system is always located at a stable equilibrium state. Because, the adiabatic theorem holds well in the tip-surface system of FFM as mentioned in Section 2.2.

Based on the assumptions mentioned above, the tip apex atom is always located at an equilibrium position of the potential surface as shown in Figure 15 for each cantilever basal position. Therefore, it is implicitly assumed that the energy of the system is supplied or removed instantaneously by the external force driving the cantilever. The potential energy surface of the tip-surface system for a given cantilever basal position is very slowly changed in time with the scan of the cantilever. It is noted that the adiabatic potential surface itself evolves in time by the external force driving the cantilever. This evolution is schematically understood by a simple one-dimensional model as shown in Figure 15. In this figure, it is assumed that $V(x) = V_T(x) + V_{TS}(x)$. And the coordinate x of the tip apex atom is taken in the cantilever scan direction. By changing the stiffness of the cantilever, two types of the potential energy surfaces appear as shown in Figs. 15(a) and 15(b). For the stiff cantilever, the total energy V is nearly parabolic and only single minimum appears. However, for the soft cantilever, several metastable points corresponding to local minima appear. Thus the appearance of the case of

Fig. 15(a) or Fig. 15(b) is determined by the ratio between the magnitude of the spatial variation of V_T and V_{TS}.

Therefore, for the stiff cantilever, the representative point of the system (the tip atom in this case) is always moving trapped in the single minimum of the potential energy surface and shifts continuously as shown in Fig. 15(a). On the other hand, for the soft cantilever, discontinuity of the motion of the tip atom occurs as shown in Fig. 15(b). In this case, for some period of the cantilever scan, the tip atom is moving continuously. But it makes a sudden jump from one minimum to another deeper minimum, when the barrier between two minima disappears. The energy of the FFM system is dissipated instantaneously when the tip atom slips from a local potential minimum to another. This mechanism of energy dissipation mentioned above is a Tomlinson's mechanism. We discuss various features of atomic-scale friction based on this mechanism.

3.3. Comparison between simulation and experiment

Figure 16 shows the comparison between the simulated and the experimental FFM images of F_x/k_x and F_y/k_y for the case that the cantilever is scanned in the x-direction. Both the simulation and the experiment are performed under the constant-height and the repulsive-force mode. In the numerical simulation, the lateral components of the spring constant are fixed as $k_x = k_y = 2.5$ N/m, and z_s is varied. As the cantilever basal position approaches the surface, z_s decreases, and the average value of F_z, $< F_z >$, increases. Further, detailed experimental setup is described in Fujisawa *et al.* [20]. In Fig. 16, simulated image patterns reproduce fairly well experimental ones.

Here, the load of simulation [$< F_z >$=1.42 nN] is by two orders of magnitude smaller than that of the experiment [$< F_z >$=327 nN]. This is due to the fact that we adopt a single-atom tip model in the simulation. Abraham *et al.* [22] pointed out that the flake tip actually detects force on the graphite surface in contact-AFM experiments. Therefore, if the calculation is performed by the flake tip including a large number of carbon atoms, a magnitude of the load in the simulation becomes as large as that in the experiment.

3.4. Analysis of FFM image

As shown in the last section, similar features of patterns are obtained in both the simulated and the experimental images. Therefore, in this section, we clarify the physical meaning of these patterns, by using an analytical method whose concept is presented by Gyalog *et al.* [21].

3.4.1. Method of Analysis

The method of analysis is described below in detail. First the potential V is converted from the function of three variables, x, y and z, into a function of two variables, x and y. For that purpose z should be chosen as the point corresponding to the minimum of V, satisfying,

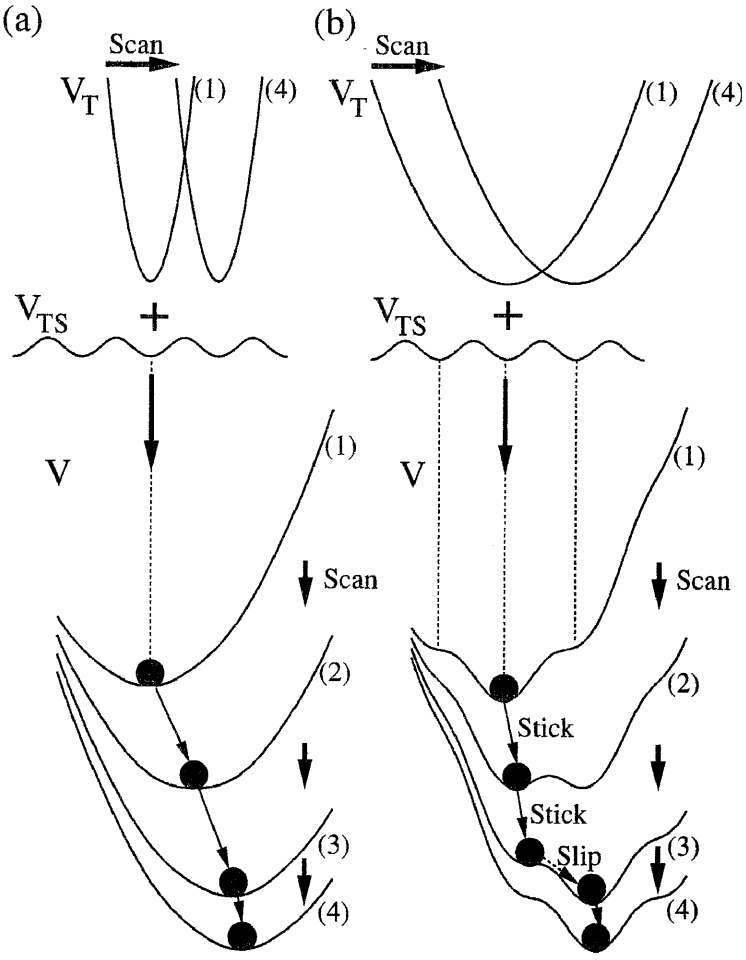

Figure 15. Schematic illustration of the total energy V obtained by the sum of the elastic energy of the cantilever spring V_T and the tip-surface interaction V_{TS}. Two cases for a (a) stiff and (b) soft cantilever are presented. (1)-(4) denote the time evolutions of the potential by the cantilever scan. For the stiff cantilever, total energy V is nearly parabolic, and the tip atom (the shaded circle) is always located at the minimum. However, for the soft cantilever, several metastable points corresponding to local minima appear, and the tip atom jumps to the deeper minimum at these points, when the barrier between two minima disappears.

$$F_z = -\frac{\partial V_{TS}(x,y,z)}{\partial z} = k_z(z - z_s). \tag{11}$$

The solution z of eq.(11) can be obtained as $z(x,y;z_s)$. V is therefore represented as

$$V(x,y;x_s,y_s,z_s) = \frac{1}{2}(k_x(x-x_s)^2 + k_y(y-y_s)^2) + V'(x,y;z_s), \tag{12}$$

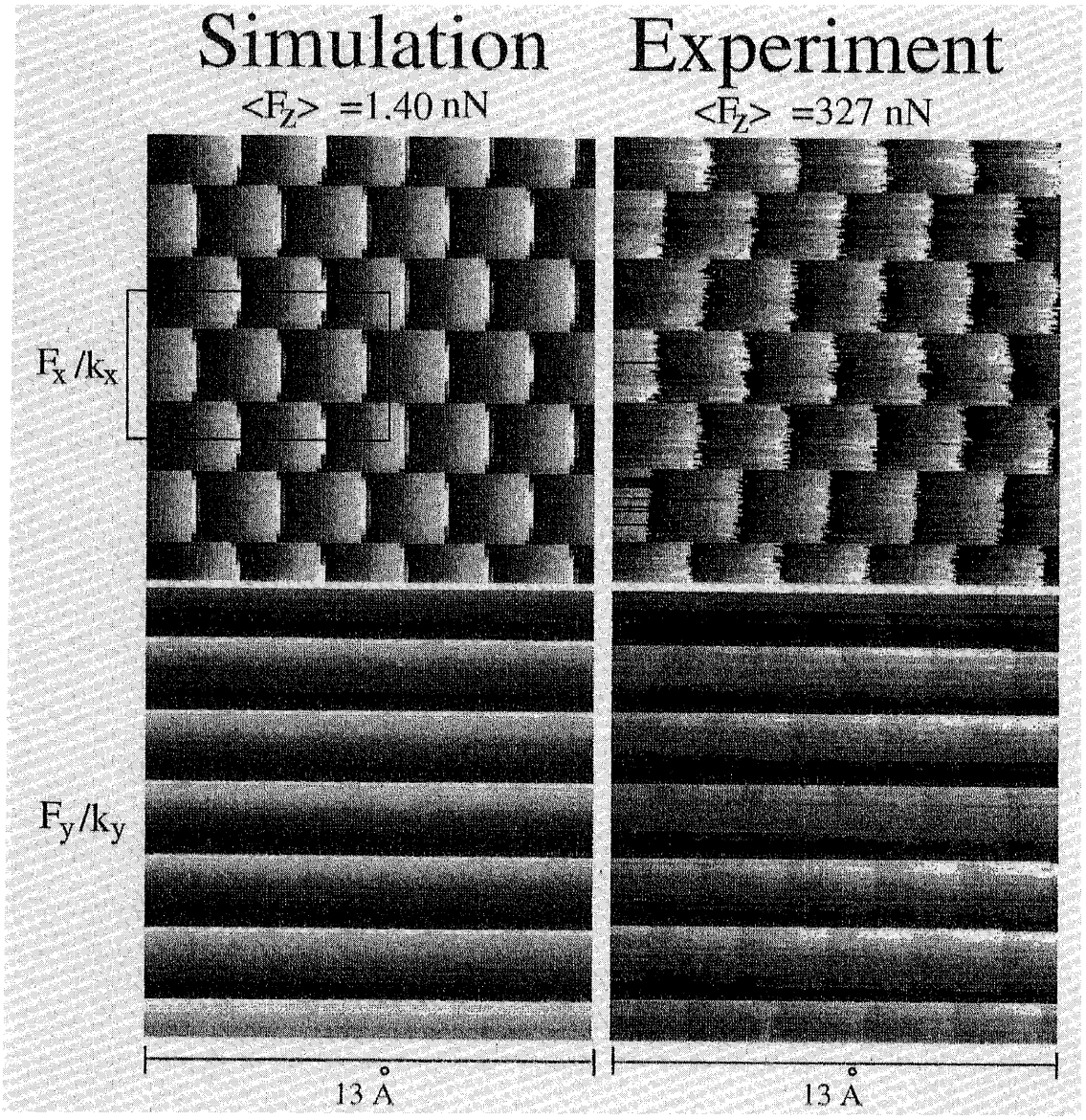

Figure 16. FFM images of F_x/k_x and F_y/k_y obtained by numerical simulations and experiments with a tip scanned in the x direction of Fig. 14.

where

$$V'(x,y;z_s) = \frac{1}{2}k_z(z(x,y;z_s)-z_s)^2 + V_{TS}(x,y,z(x,y;z_s)). \quad (13)$$

In the next step the lateral coordinates of the tip atom, x and y, can be determined by

$$\nabla_i V = 0 \quad (i=x,y), \quad (14)$$

for each cantilever basal position $(x_s, y_s, z_s + l_0)$.

To satisfy the quasi-stable equilibrium condition of the two-dimensional position of the tip atom (x,y), it is necessary that Hessian of V is positive definite. Therefore the relation:

$$|\partial^2 V/\partial x_i \partial x_j| > 0 \quad (i,j=x,y) \quad \text{and} \quad \partial^2 V/\partial x^2 > 0, \quad (15)$$

is required in addition to eq. (14).

Further, the equilibrium condition, eq. (14), can be rewritten as follows:

$$(x_s, y_s) = \left(x + \frac{1}{k_x}\frac{\partial V'(x,y;z_s)}{\partial x}, y + \frac{1}{k_y}\frac{\partial V'(x,y;z_s)}{\partial y}\right). \quad (16)$$

Eq. (16) is the condition of the lateral components of the cantilever basal position (x_s, y_s) which can realize the equilibrium tip atom position (x,y).

Thus the quasi-stable equilibrium region of the two-dimensional tip atom position (x,y) is obtained, and it is mapped to a domain of the cantilever basal position (x_s, y_s). It should be noted that the mapping to (x_s, y_s) from (x,y) is monovalent, but the inverse mapping to (x,y) from (x_s, y_s) is not necessarily monovalent.

3.4.2. Stable tip atom domains

The region of the stable atom position (x,y), where the real solution (x_s, y_s) of eq. (15) exist, changes with the value of z_s. Under the low loading condition (for

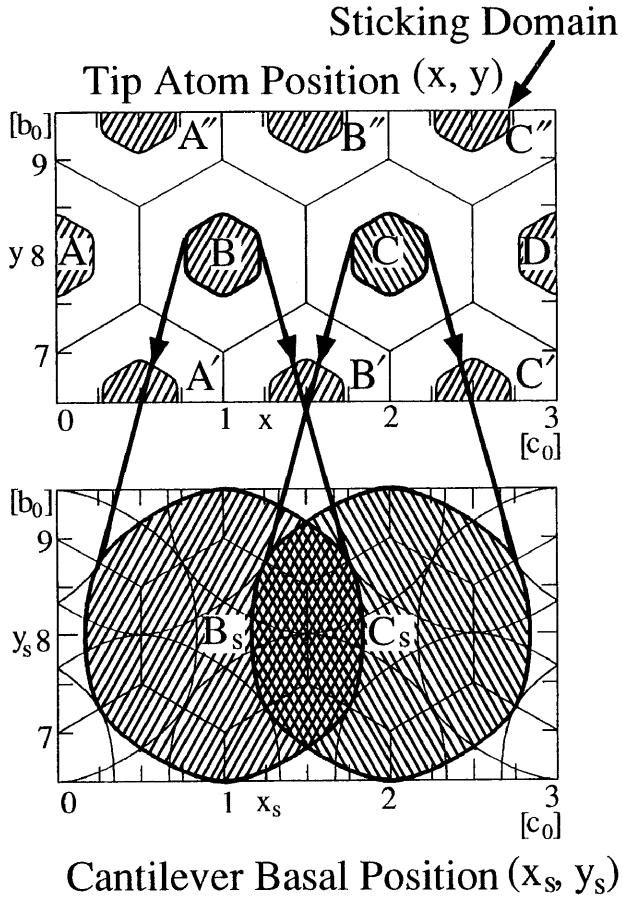

Figure 17. The mapping relation between (x, y) and (x_s, y_s) for $< F_z >= 1.42$ nN. A top figure represents sticking domains A–D, A′–C′, and A″–C″ in the (x, y) space indicated by hatched regions. By eq. (3-6), each sticking domain is mapped into a domain in the (x_s, y_s) space, as shown in the bottom figure. The mapping relation between domains B_s or C_s, and the sticking domains B or C, are clearly shown. Solid lines represent C-C bonds of the graphite surface. The region of these figures is $0 \leq x \leq 3\ c_0$ and $6.5\ b_0 \leq y \leq 9.5\ b_0$, corresponding to the region surrounded by a framework in Fig 16. Here $c_0 = 2.46$ Å, and $b_0 = 1.42$ Å.

large z_s), the region covers the whole (x, y) space. However, as the load is increased in the frictional-force regime (with the decrease of z_s), the region becomes to be separated into mutually disconnected domains. Hatched domains B and C in Figure 17 show disconnected stable domains of the tip atom (x, y). Fig. 17 corresponds to a region within the box in a simulated image of Fig. 16. The tip atom moves discretely between hatched domains. Therefore we call such domains as B and C, "sticking domains", hereafter. Thus the exact boundary of the sticking domain can be clearly defined based on eq. (15).

Each sticking domain is mapped into a domain in the (x_s, y_s) space, by eq. (16), as shown in Fig. 17. It is assumed that the sticking domains A–D, A′–C′ and A″–C″ are mapped into the domains A_s–D_s, A'_s–C'_s and A''_s–C''_s, respectively, hereafter. In the frictional-

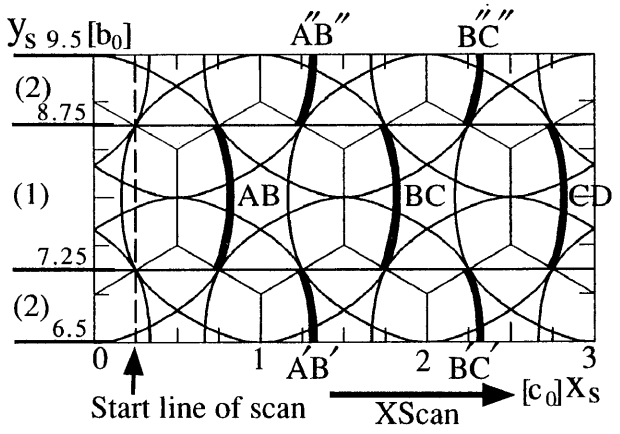

Figure 18. Thick curves, AB, BC, CD, A′B′, B′C′, A″B″ and B″C″, represent analytically predicted fringes of FFM image patterns for the x scan. Two different types of FFM image appear. Solid lines represent C-C bonds of the graphite surface. Start line of scan ($x = 0.25\ c_0$) is also shown by broken lines.

force regime, although the function defining the mapping $(x_s(x, y), y_s(x, y))$ is univalent, its inverse relation $(x(x_s, y_s), y(x_s, y_s))$ is generally multivalent. Therefore the mapped domains in the (x_s, y_s) space are partly overlapped with some other mapped domains. In Fig. 17, mutually overlapping domains B_s and C_s in the (x_s, y_s) space, which are the maps of the sticking domains B and C in the (x, y) space, are clearly shown by hatched regions.

3.4.3. Predicted fringe of FFM image patterns

In the simulation, it is assumed that no lateral deviation exists between (x, y) and (x_s, y_s), for the initial scan condition. Therefore, the initial position of the tip atom is the hollow site which is the center of the honeycomb lattice where the start line of the scan exists. While the cantilever basal position is scanned, the tip atom continuously moves within the sticking domain. Here we set a simple assumption as follows: When the cantilever basal position comes to the boundary of the sticking domain in the (x_s, y_s) space, the tip atom discretely moves into the sticking domain in the (x, y) space, whose center is the nearest hollow site to the present cantilever basal position. Then, the cantilever basal position on the boundary of the domain in (x_s, y_s) plane, is marked as the part of the image fringe between the bright and the dark area along the scan direction.

Based on this assumption, fringes of FFM image patterns for the x scan are predicted by the thick curves as shown in Figure 18, where two different types of image fringe appear as follows: region (1) of $7.25\ b_0 \leq y \leq 8.75\ b_0$, and region (2) of $6.5\ b_0 \leq y \leq 7.25\ b_0$ or $8.75\ b_0 \leq y \leq 9.5\ b_0$. For example, the tip atom motion in the case that the starting position exists within a region (1), is considered. The tip atom (x, y) exists within a domain A in Fig. 17, for the initial state of scan. When the cantilever basal position comes to the

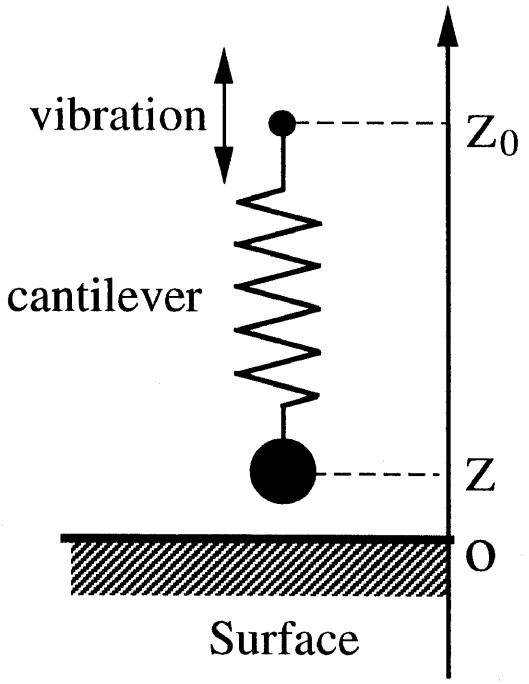

Figure 19. The cantilever-tip system is mimicked by a material point connected with one-dimensional spring.

boundary of the domain 'A_s' in the (x_s, y_s) space, the tip atom discretely moves from the sticking domain 'A' into the sticking domain 'B' in the (x, y) space, whose center is the nearest hollow site to the present cantilever basal position. Therefore, for all the x scan within the region (1), the discrete jump of the tip atom from the domain A to the domain B, occurs, and, a thick curve AB, a part of boundary of domain A_s, appears as a fringe of an FFM image pattern. For the case of region (2) in Fig. 18(b) and all the cases of Fig 18, just the same explanation as mentioned above can be done.

Thus it is clarified that, not all of, but some part of boundaries of the domains in the (x_s, y_s) space are observed in the FFM image. Which part of the boundary of the domain in the (x_s, y_s) space is actually observed, is determined by the scanning direction.

4. Dynamics of the cantilever in noncontact AFM

In this section, we discuss some results of preliminary calculations of the dynamics of the cantilever of a noncontact AFM. In the numerical simulation, the system comprised of the cantilever and the tip is mimicked by a mass point connected with a spring as shown in Figure 19.

Here the cantilever vibration can be expressed by a forced vibration of the mass point around the equilibrium position with repeated collisions with the surface in a certain condition. The collision itself is governed by the microscopic response of the atoms in the tip and the surface in the touching region. Through this process the local microscopic information is picked up by the

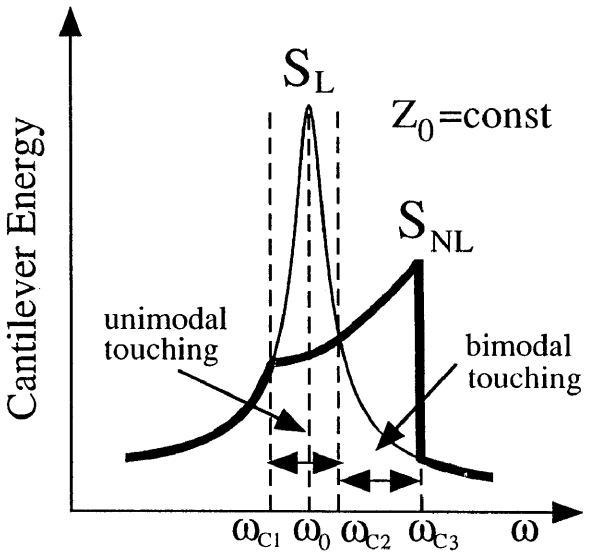

Figure 20. Schematic illustration of the energy spectrum. The relation between ω/ω_0 and cantilever energy is presented. Two kinds of energy spectra for linear and nonlinear are shown.

cantilever. In order to investigate the effect of the collision, *i.e.*, the touching process between the mass point and the surface on the macroscopic motion of the cantilever, we made a numerical simulation with assuming Lennard-Jones potential as the tip-surface interaction. If only the motion along the vertical z direction is considered, the cantilever-surface system is described by a differential equation as follows:

$$\ddot{Z} + \frac{\omega_0}{Q}\dot{Z} + {\omega_0}^2(Z - Z_0) + C\left[\left(\frac{\sigma}{Z}\right)^7 - \left(\frac{\sigma}{Z}\right)^{13}\right] = {\omega_0}^2 A \sin(\omega t), \quad (17)$$

where, Z is a vertical coordinate of the material point, and Z_0 is an equilibrium position. Further, ω_0 is a resonant frequency of the cantilever, ω and A are frequency and amplitude of the external force. C is a parameter of the Lennard-Jones potential. In the simulation, the above parameters are fixed as follows: $\omega_0 = 1$, $Q = 10$, $C = 12$, $\sigma = 0.5$, $A = -0.2$. ω and Z_0 are assumed as parameters.

By solving eq.(17) for each ω/ω_0, the stationary oscillation state is obtained. Figure 20 shows energy spectra with and without nonlinear tip-surface interaction. In the absence of the tip-surface interaction, or in the case where the tip height is significantly large, the Lorenzian type spectrum S_L corresponding to a normal forced vibration appears. However, when the tip-height is decreased, a remarkable feature appears in the spectrum S_{NL} as follows:

For $\omega \ll \omega_0$, energy spectrum S_{NL} is just the same as S_L. In this case, the cantilever does not touch the surface during vibration. However, for the specific case of $\omega = \omega_0/n$ $(n = 2, 3, \ldots)$, the cantilever touches the surface by the period which is n times as much as $2\pi/\omega_0$. We call this strange type of resonance 'fractional reso-

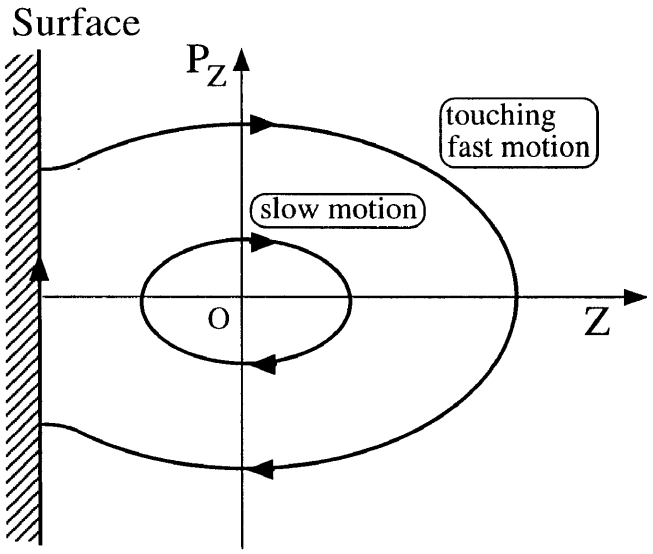

Figure 21. Schematic illustration of bi-modal states within phase space: (1) non-touching slow motion (2) touching fast motion.

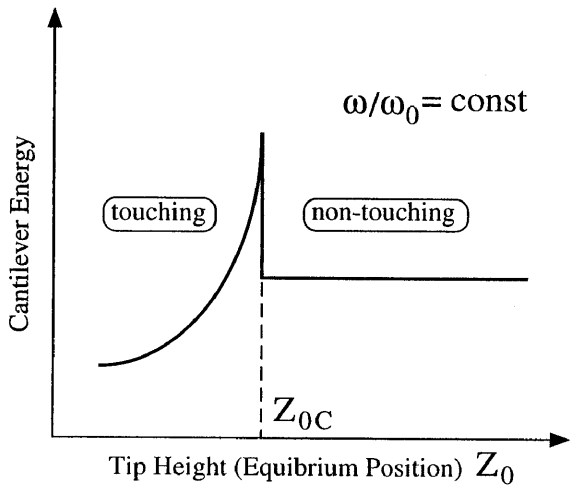

Figure 22. Schematic illustration of the energy spectrum. The relation between the tip height (equilibrium position) Z_0 and cantilever energy is presented.

nance'. For $\omega \simeq \omega_0$, above a critical frequency number ω_{C1}, S_{NL} discretely deviates from S_L, and the cantilever comes to touch the surface. Under the stationary vibration, the cantilever touches the surface once during one period. The oscillation amplitude for S_{NL} becomes smaller than that for S_L. In this case the cantilever takes a "unimodal touching", since there is only a single state of dynamic motion, as contrast to the neighboring higher frequency region. As ω is increased over the frequency ω_{C2} where S_{NL} crosses S_L, the bimodal touching regime appears. In this frequency region, two kinds of oscillation modes are possible. These two modes are switched from time to time by a little change of the initial condition or stochastic forces from the surface. These two modes are schematically presented in the phase space in Figure 21. As ω is further increased above a critical frequency number ω_{C3}, a jump of the energy spectrum occurs, and S_{NL} becomes the same as S_L again. The cantilever takes only the non-touching motion.

Further, the effect of the cantilever height (equilibrium position) from the surface Z_0 is investigated. Figure 22 presents a relation between Z_0 and the cantilever energy. Above a critical value of Z_{0C}, the energy is kept constant, which means that the cantilever takes a non-touching motion. However, with the decrease of Z_{0C}, the energy discretely increases at the point $Z_0 = Z_{0C}$, and then it gradually decreases with Z_0. In this case, the cantilever takes a large amplitude touching motion, just with the same condition as the small amplitude non-touching motion. Therefore the former might be called as the "dynamic touching" of the tip to the surface.

5. Conclusions

In this article, we performed a systematic study about the mechanism of AFM, based on both a theoretical simulation and an analytical method.

First in Section 2, physical meaning of contact AFM images in the repulsive force mode is clarified. From this calculation, several fundamental features of the effects on the contact AFM images are systematically clarified. Generally speaking, contact AFM images represent not only the surface geometrical structures, but also are influenced by many other microscopic features of the tip and the surface such as the force distributed over atoms in the contact region, deformation, tip apex structure, and orientation.

Secondly in Section 3, fundamental feature of atomic-scale friction appearing in FFM images is investigated. Simulated FFM images are in good agreement with experimental ones. Then, based on an analytical method, general features of the FFM images of graphite surface can be completely understood. There exists a mapping relation between the tip atom position (x, y) and the cantilever basal position (x_s, y_s). In the frictional-force regime, disconnected domains in the (x, y) space can be defined as sticking domains. It is clarified that part of the boundary of domain in the (x_s, y_s) space into which the domain in the (x, y) space is mapped, appears as a fringe of FFM image between the bright and the dark area along the scan direction. This analysis gives a clear explanation to both simulated and experimental FFM images.

Lastly in Section 4, it is clarified that the collision between the tip and the surface gives a significant influence on the large amplitude cantilever oscillation in nc-AFM. Especially, there exists a region where both the touching and the non-touching motion appear, depending on the initial condition and the stochastic forces from the surface. It can be thought that the dynamical touching of the cantilever with the surface plays an important role for obtaining an atomic-resolution of nc-AFM.

Acknowledgement

The authors thank Dr. S. Fujisawa (Mechanical Engineering Laboratory, Japan), Prof. Y. Sugawara (Osaka University, Japan), and Prof. S. Morita (Osaka University, Japan), for giving them experimental data used in Section 3 and having many fruitful discussions. They also thank T. Gyalog (University of Basel, Switzerland), for his very constructive suggestions about interpretations of FFM images. This work is partially supported by a Grant-in-Aid from the Ministry of Education, Science and Culture. The numerical calculations were performed by HITAC S-3800 at the Computer Center of the University of Tokyo.

1) G. Binnig, C. F. Quate and Ch. Gerber: Phys. Rev. Lett. **56** (1986) 930.
2) N. Sasaki and M. Tsukada: Jpn. J. Appl. Phys. **34** (1995) 3319.
3) N. Sasaki and M. Tsukada: Phys. Rev. B **52** (1995) 8471.
4) C. M. Mate, G. M. McClelland, R. Erlandsson and S. Chiang: Phys. Rev. Lett. **59** (1987) 1942.
5) N. Sasaki, K. Kobayashi and M. Tsukada: Surf. Sci. **357-358** (1996) 92.
6) N. Sasaki, K. Kobayashi and M. Tsukada: Phys. Rev. B **54** (1996) 2138.
7) N. Sasaki, K. Kobayashi and M. Tsukada: Jpn. J. Appl. Phys. **35** (1996) 3700.
8) N. Sasaki, K. Kobayashi and M. Tsukada: NATO-ASI Series, *Micro/Nanotribology and its Applications*, ed. B. Bhushan (Kluwer Academic Publishers, Dordrecht, 1997), 355.
9) N. Sasaki, M. Tsukada, S. Fujisawa, Y. Sugawara, S. Morita and K. Kobayashi, J. Vac. Sci. & Technol. B. (1997) in press.
10) Q. Zhong, D. Inniss and V. B. Elings: Surf. Sci. **290** (1993) L688.
11) W. A. Harrison: *Electronic Structure and the Properties of Solids: The Physics of the Chemical Bond* (W. H. Freeman and Company, San francisco, 1980), pp.193-197
12) A. Yoshimori and Y. Kitano: J. Phys. Soc. Japan **2** (1956) 352.
13) S. A. C. Gould, K. Burke and P. K. Hansma: Phys. Rev. B **40** (1989) 5363.
14) W. H. Press, S. A. Teukolsky, W. T. Vetterling and B. P. Flannery: *Numerical Recipes: The Art of Scientific Computing* 2nd ed. (Cambridge University Press, New York, 1992), pp.413-418.
15) H. Tang, C. Joachim and J. Devillers: Surf. Sci. **291** (1993) 439.
16) G. Binnig, Ch. Gerber, E.Stoll, T. R. Albrecht and C. F. Quate: Europhys. Lett. **3** (1987) 1281.
17) T. R. Albrecht and C. F. Quate: J. Vac. Sci. Technol. A **6** (1988) 271.
18) H. Schmidt, J. Heil, J. Wesner and W. Grill: J. Vac. Sci. Technol. A **8** (1990) 388.
19) G. A. Tomlinson: Phil. Mag. **7** (1929) 905.
20) S. Fujisawa, E. Kishi, Y. Sugawara and S. Morita: Tribo. Lett. **1** (1995) 121.
21) T. Gyalog, M. Bammerlin, R. Luthi, E. Meyer and H. Thomas: Europhys. Lett. **31** (1995) 269.
22) F. F. Abraham and I. P. Batra: Surf. Sci. **209** (1989) L125.